Ignition and Combustion Characteristics of Al/TiB 2 -Based Nanothermites: Effect of Bifuel Distribution

Vidushi Singh, Tao Wu, Ludovic Salvagnac, Alain Estève, Carole Rossi

Ignition and Combustion Characteristics of Al/TiB_2 Based Nanothermites : Effect of Bi-Fuel distribution

Vidushi Singh[1], Tao Wu[1], Ludovic Salvagnac[1], Alain Estève[1], Carole Rossi[1,]*

[1]LAAS-CNRS, University of Toulouse, 7 Avenue du Colonel Roche, 31400 Toulouse, France

[*]*Corresponding Author*

Carole Rossi

LAAS-CNRS

7, Avenue du Colonel Roche, 31400 Toulouse, France

Tel.: +33 56 133 6301

E-mail address: carole.rossi@laas.fr

Keywords: Titanium diboride, thin-films, reactive materials, ignition and combustion, nanolaminates

Abstract

Aluminum has demonstrated compelling attributes over decades of research, encompassing affordability, abundance and a high specific energy density when utilized as a fuel in energetic materials such as nanothermites. However, combustion performance of Al suffers from its high ignition point and sintering tendency, the latter being hypothesized to be the rate-limiting step in Al-based nanothermite combustion. Herein, we examine the influence of nano-TiB_2 addition on the ignition and combustion properties of CuO/Al by adjusting the Al-TiB_2 binary fuel distribution. Magnetron sputtered CuO/Al-TiB_2 multilayers were prepared and their ignition and combustion characteristics were studied. It was found that all configurations of CuO/Al-TiB_2 system outperform CuO/Al. Notably, 62.5% loading demonstrated the most significant improvement in the ignition delay, with a decrease of ~ 100%. Furthermore, each nano TiB_2-loaded CuO/Al thermite exceeded the propagation rate of CuO/Al by a factor of 2. Differential scanning calorimetry, high-speed videography, spectroscopy and microscopy were instrumental in elucidating the factors contributing to this improvement and understanding the role of TiB_2. While a low temperature TiB_2 oxidation contributed to shorter ignition delays, the combustion characteristics were found to be highly controlled by heterogeneous gas-condensed phase reaction rather than the flame temperature and materials' thermal properties. This study demonstrates that the addition of nano-TiB_2 to Al-based thermites holds a significant potential in the applications where it is necessary to either lower or finely tune the ignition times. From a manufacturing perspective, this integration technique provides a straightforward approach to enhance the ignition and combustion performance CuO/Al nanothermites.

1. Introduction

Energetic materials, made from highly reactive metal fuels (Al, Mg, B) and metal oxide particles (CuO, MoO_3, Fe_2O_3, Bi_2O_3) of sizes around $10^2 – 10^3$ nm, known as nanothermites, have many commercial and research applications. These materials release a significant amount of energy with low gas release despite their small size. Nanothermites are therefore explored to provide intense, controllable and efficient energy release in small packages [1,2] making them valuable in a wide range of pyrotechnic applications including cutting and welding [3], initiation [4–6], actuation [7–11], chip destruction and propulsion [8,12–14]. There is continuing research effort in the area of nanothermites' properties and their applications with a special focus on improving their performance, safety and industrial utility.

Aluminum (Al) stands out as the most extensively studied metallic fuel, owing to its high reaction enthalpy (84 kJ/cm3, 31 kJ/g), widespread availability, cost-effectiveness and non-toxic nature. However, despite its thermodynamic advantages, Al faces a challenge in the form of a high ignition point, primarily attributed to the presence of its native oxide. This has led to the pursuit of various physical or chemical modifications of Al-Al_2O_3 core-shell microstructure, aiming to lower aluminum's ignition temperature and consequently enhance the thermite ignition and combustion. In addition, thermal or plasma pre-treatment [15–17] in Al microstructures have shown to lower the initiation onset and the burn time. Because mass transport is a key factor in setting the reaction pathway and hence regulating the ignition point, several other studies have been populated by approaches modifying the native Al_2O_3 using polymeric material [18,19] or different oxides [20,21]. While all these strategies prove categorically effective, it is undeniable that they require time-consuming and cost-ineffective engineering efforts.

The combination of Al with other metallic or metalloid fuels has been considered an aspirational approach to modify the reaction pathway, thereby influencing both the ignition and the combustion processes in nanoscale energetic composites. While Al burns mostly in the vapor phase, metals such as Ti (boiling temperature of 3300 °C) burns in a condensed phase. Zhao et. al demonstrated species transfer across a boundary between two molten or solid materials in Al-Ti system resulting in a dual phase combustion regime with an improved efficiency [22]. Nevertheless, Al-Ti (with CuO oxidizer) was reported to be a considerably sensitive nanothermite, accompanied by significant fabrication and safety challenges [23]. Boron is another fuel of interest [24–26] due to its relatively higher gravimetric and volumetric reaction enthalpies (~140 kJ/cm^3, ~60 kJ/g), but the associated kinetic constraints discourage its use [27]. The natively occurring B_2O_3, with a low melting point at ~450 °C, presents itself as a major barrier to oxygen diffusion [28,29]. However, B as an additive has been reported to boost the reactivity of Al/CuO thermites up to three times, elevating the reaction temperatures beyond the boiling point of B_2O_3 [30]. More recently, TiB_2 as an additive fuel in Al/CuO was demonstrated as a promising strategy to enhance the ignitability of Al/CuO thermites and accelerate the reaction kinetics [31]. TiB_2 in direct contact with CuO significantly enhances the decomposition of the latter at temperatures as low as 280 °C. Moreover, B_2O_3 reportedly reacts with Al at temperatures above ~ 620 °C, leading to the oxidation of Al accompanied by heat release, as well as the release of free B [32]. Understanding the heats of reaction in a ternary system, given the simultaneous activation of various reactions, is complex. However, this complexity opens doors to a myriad of opportunities towards the tunability of energetic properties in titanium diboride integrated nanothermites.

The objectives of this study are two-fold: (i) to investigate the impact of nano-TiB_2 addition on the energetic properties of Al/CuO nanothermites by adjusting the distribution of the fuel concentrations between TiB_2 and Al and, (ii) to gain deeper insights into ignition and combustion

processes of the resulting CuO/Al-TiB_2 thermite. To conduct this study, we utilized magnetron sputtering to grow high-purity and well-defined CuO/Al-TiB_2 nanothermites. Contrary to the powdered thermites, magnetron sputtering technique provides ideal model systems with precise control over the sizes, ratios and mixing of the reactants (fuel and oxidizer). CuO was selected as the oxidizer due to its relative stability in ambient conditions, ease of sputtering, and its established use as the source of oxygen in nanoscale thermite reactions [33–35].

The ignition and the combustion performances of CuO/Al-TiB_2 multilayers, adjusted to various TiB_2 loadings, are characterized in open air conditions and subsequently compared to the reference CuO/Al. Each CuO/Al-TiB_2 sample configuration exhibits more than 95% improvement in the ignition delay. By microscopically imaging the propagation front and characterizing the post-combustion products, this study investigates the fundamental aspects of combustion dynamics in CuO/Al-TiB_2 ternary thermite system. Our experimental findings reveal that the burning of TiB_2 in condensed phase leads to the formation of a glassy surface matrix (composed of TiO_x and B_2O_3) that captures the burning Al particles to the proximity of the surface, promoting efficient heat transfer from the high temperature flame front to the unburnt thermite. This, in turn, leads to enhanced propagation rates, unlike CuO/Al. This work not only offers insights into the energetic properties of Al-TiB_2 binary fuel, but also provides straightforward and effective technological methods for tailoring the ignition and the combustion properties of Al-based nanoscale energetic composites to meet diverse application needs.

2. Materials and methods

2.1 Sample preparation

Each of the three nanolayers of CuO, Al and TiB_2 were sputter deposited using Direct Current (D.C.) magnetron sputtering with a sputtering tool from Thin Film Equipment (TFE), Italy,

utilizing 8 by 3 square inches and ¼ inch thick targets from Neyco, France. The base pressure was set to 5×10^{-7} Torr. For CuO nanolayer, the oxygen and argon gas flow were set to 19.2 and 32 s.c.c.m. The sputtering parameters can be found in **Supporting Information, Table S1**. The unbiased sample holder was centered at 15 mm from the target. Further information about the sputtering process can be found in our previous works [23,36].

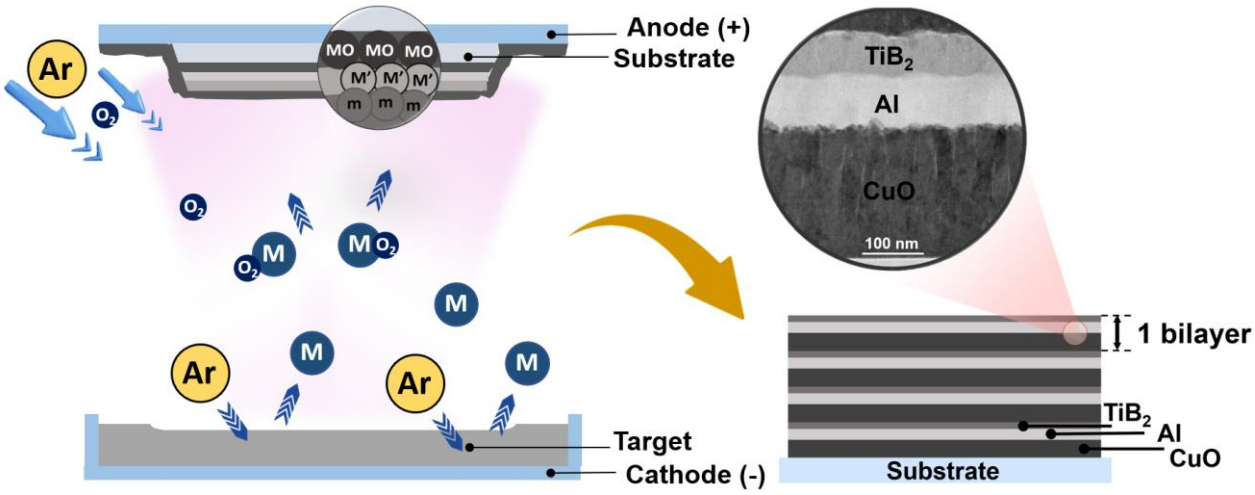

Figure 1. Schematic magnetron sputtered CuO/Al-TiB_2 multilayers. The deposition begins with CuO, followed by Al and TiB_2 nanolayers, together CuO-Al-TiB_2 being referred to as one bilayer

Various CuO/Al-TiB_2 multilayers were prepared to perform a head-to-head comparison. Each sample was composed of 10 bilayers (BL) of CuO/Al-TiB_2 starting with CuO followed by the deposition of the Al-TiB_2 layer as shown in **Figure 1**. Al-TiB_2 notation represents the deposition of Al (over CuO) followed by that of TiB_2 over Al. The CuO layer thickness is set to 200 nm. It is assumed that CuO is fully consumed during the redox reaction with both Al and TiB_2 fuels. The distribution of Al-TiB_2 bi-fuel concentrations varies across different CuO/Al-TiB_2 multilayer samples based on the following chemical reactions:

$$2\ Al + 3\ CuO \rightarrow 2\ Al_2O_3 + 3\ Cu$$

$TiB_2 + 5\ CuO \rightarrow TiO_2 + 5\ Cu + B_2O_3$

The fuel-to-oxidizer ratio (equivalence ratio) is maintained at 2 for both the above reactions. The percentages in CuO/Al-TiB_2 x% in **Table 1** denote the volume percent of CuO that will theoretically be consumed by TiB_2 in a fuel-rich configuration. For simplicity, x% is referred to as TiB_2 loading. For example, 25% TiB_2 loading means that 25% of 200 nm CuO is consumed in CuO/TiB_2 redox reaction, while the rest 75% of CuO reacts with Al in CuO/Al-TiB_2 system. The thickness of each nanolayer is carefully controlled via a calibration process preceding each full stack deposition. For comparison purposes, two reference samples of CuO/Me {Me: Al, TiB_2} were also fabricated wherein the thicknesses of CuO, Al and TiB_2 were set to 200 nm, 200nm and 100 nm corresponding to a fuel-rich (Me:CuO = 2) configuration to maintain the consistency throughout.

Table 1. Thicknesses of each of the three, CuO, Al and TiB_2 nanolayers corresponding to different TiB_2 loading (percent)

Sample name	TiB_2 loading (%)	Thickness (nm)			n (molar ratio of TiB_2 and Al)
		CuO	Al	TiB_2	
CuO/Al	0	200	200	-	-
CuO/Al-TiB_2 25%	25	200	159	25	0.1
CuO/Al-TiB_2 50%	50	200	106	49	0.3
CuO/Al-TiB_2 62.5%	62.5	200	80	62	0.5
CuO/Al-TiB_2 75%	75	200	53	74	0.9
CuO/TiB_2	100	200	-	100	-

Free-standing 10 BL of CuO/Me {Me: Al, TiB_2, Al-TiB_2} foils were also fabricated for auto-ignition temperature characterization and thermal analysis. A silicon wafer was plasma cleaned before being spin-coated with a layer of photoresist (NLOF, 5 μm). Succeeding a post-exposure

110 ˚C baking step, the multilayers were sputtered onto the wafer. The foils were then lifted-off in DMSO and rinsed.

2.2 Exothermic reaction characterization in neutral atmosphere

The heat released during each step of the chemical reaction in the multilayers is characterized by thermal analysis performed in Ar atmosphere using differential scanning calorimetry (DSC) carried out in a NETZSCH DSC 404 F3 Pegasus system equipped with a DSC-Cp sensor type S and a platinum furnace. The thermogram, normalized to the foil mass (typically ~5 mg), was recorded at a constant heating rate of 10 °C per minute up till 950 °C. Prior to running each sample, a blank run was performed to correct the baseline after each measurement. The heat released as a result of each exothermic event was determined by the area under the associated DSC peak.

2.3 Ignition characterization

Auto-ignition temperature - ~ 2 mg of CuO/Me {Me: Al, TiB_2, Al-TiB_2} foils were dropped onto the hot plate (Wenesco, USA) and the auto-ignition temperature was recorded when a flash was detected immediately upon contact between the foils and the surface of the hot plate. The hotplate was held at each temperature sufficiently long enough to stabilize at that temperature before dropping the foils.

Ignition delay - The multilayers were ignited under ambient conditions using externally applied direct current pulse through the Ti filament of the chips as presented in the previous works [23,31]. Briefly, a simple photolithography process was used to define a 300 nm Ti resistance. Thereafter, 350 nm thick Au was evaporated onto the surface and subsequently patterned to identify the contact pads as well as the resistive filament. 10 BL CuO/Me {Me: Al, TiB_2, Al-TiB_2} were then sputter deposited through a shadow mask onto the Ti resistance (**Supporting Information, Figure S1a**).

For each test, the current was adjusted so as to keep the same dissipated power (6.125 W). The ignition delay was measured using a photodiode (VISHAY, BPV10) biased at 5 V placed a few centimeters away from the sample and capable of detecting the optical flash emitted from the ignition event. A 1 kΩ dummy resistance was used to measure the photocurrent. All electrical signals were acquired on a digital oscilloscope and processed using in-house programs. Ten tests were performed per sample configuration, and a mathematical average value of ignition delay (ms) was constituted. The ignition energy, calculated as the integral of power over time (up to initiation) was also calculated.

2.4 Macroscopic and microscopic imaging

The combustion behavior was investigated via two configurations of the imaging system using a high-speed camera (VEO710 Phantom, USA) recording at a sample rate of 48000 frames per second and a resolution of 512 × 64 pixels for macroscopic recording; and 14000 frames per second and a resolution of 1024 × 512 for microscopic recording. Two 10 BL CuO/Me {Me: Al, TiB_2, Al-TiB_2} thermite structures were manufactured, one with dimensions of 30 mm (length) by 2 mm (width) and other (**Supporting Information, Figure S1b**), with that of 15 mm (length) × 2 mm (width) (**Supporting Information, Figure S1c**) following the same procedure as described earlier [31]. The videoed films from multiple samples of each type were processed using the Phantom Camera Control (PCC) Cine Viewer (CV) software. The statistical values of average macroscopic burn rate were obtained by tracing the lateral movement of six locations on the flame front for each test corresponding to different configurations. Each sample was macroscopically imaged directly from the top, while the microscopic imaging was performed from both the top (direct imaging) and the bottom (indirect imaging) of the sample (looking through the glass substrate) as shown in **Supporting Information, Figure S2**. The images were processed post collection using Gwyddion

software to visualize the burning surface. The measurements on the microscopic snapshots were then performed using ImageJ software to obtain flame front widths as well as the fragments' size in each case. Additionally, to obtain a better view of the surface obstructed by fumes/particles, the collection of optical micrographs during direct imaging were aided by Cavilux HF system 810 nm emitting low power pulses (50 ns pulse duration) at a frequency of 6000 Hertz.

2.5 Characterization of products post combustion

To supplement the understanding of optical micrographs acquired during combustion, the byproducts were collected from each configuration after the combustion event. A 150 mm × 90 mm and 500 µm thick Si substrate (at ambient temperature) kept ~1 mm above the active thermite area of each sample collected the residue (**Supporting Information, Figure S3**) which was then examined for particle morphology as well as elemental composition using FEI Helios 600i DualBeam scanning electron microscope (SEM) equipped with SDD X-Max 80 mm^2 detector to perform Energy Dispersive X-Ray Spectroscopy (EDX). The images were obtained at different magnifications using backscatter electron detector to achieve better contrast. The elemental distribution of Cu, O, Al, Ti and B was then chemically mapped.

3. Results and Discussions

3.1 Ignition behavior in ambient conditions

Figure 2a shows the trend of ignition delays (ms) as a function of TiB_2 loading in CuO/Al-TiB_2 multilayers compared to CuO/Al and CuO/TiB_2 reference multilayers. TiB_2 containing CuO/Al multilayers demonstrated 100% ignition success and feature much shorter ignition delays compared to CuO/Al and CuO/TiB_2. With 25% TiB_2 loading, ignition delay is 0.36 ± 0.240 ms, ~98% lower compared to the reference CuO/Al sample (18.6 ± 3.26 ms). Further increasing the

loading to 50%, 62.5% and 75% registered 0.28 ± 0.166 ms, 0.08 ± 0.05 and 0.18 ± 0.039 ms ignition delays respectively. The shortest ignition delay is found for 62.5% TiB_2 loading, *i.e.*, a TiB_2:Al molar ratio of 0.5. Unexpectedly, for TiB_2:Al molar ratio greater than 0.5, ignition delay increases. Overall, this suggests not only a higher reactivity of CuO/Al-TiB_2 system compared to unary fuel systems (CuO/Al, CuO/TiB_2) but also offers a remarkable window of tunability of ignition delays, easily controlled via TiB_2 loading. Notably, all the measured values of ignition delay are ~50% lower than that of CuO/TiB_2 reference sample (0.76 ± 0.100 ms).

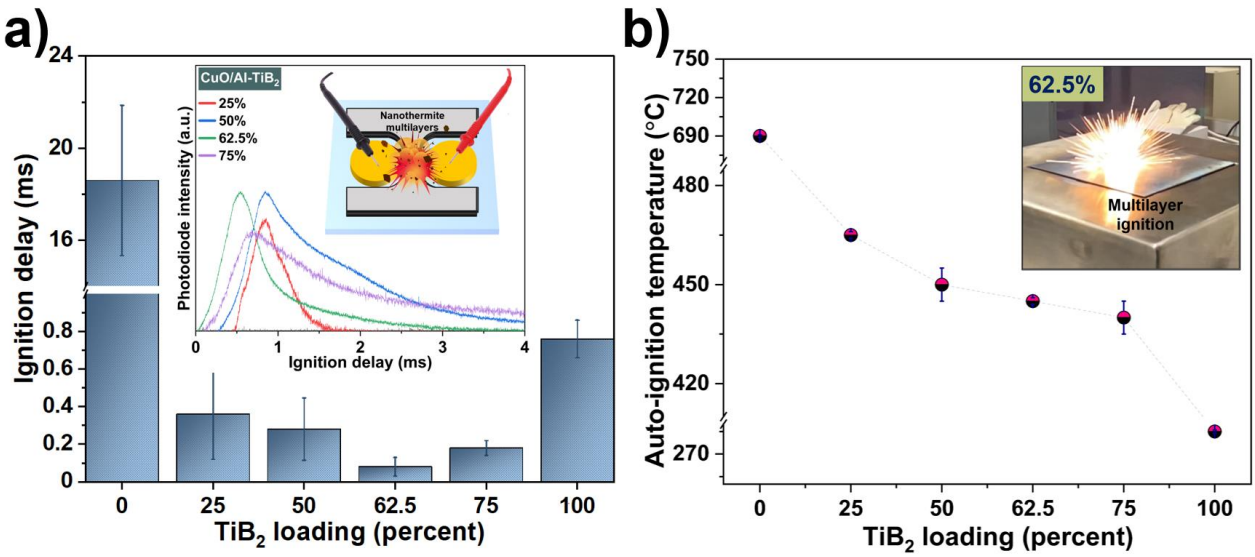

Figure 2. Characterization of the ignition parameters as a function of TiB_2 loading in CuO/Al-TiB_2: (a) ignition delay with the ignition detection signals from the photodiode shown inset (b) auto-ignition temperatures determined using hot-plate tests. Note that 0% TiB_2 loading corresponds to CuO/Al while 100% to CuO/TiB_2.

Figure 2b plots the variation in the auto-ignition temperatures obtained via hot-plate tests as a function of TiB_2 loading. All configurations of CuO/Al-TiB_2 multilayers show ignition temperatures in the range of 440 °C to 465 °C, which is significantly lower than that of CuO/Al (690 °C), CuO/TiB_2 being even lower (285 °C). TiB_2 loaded samples feature an auto-ignition

temperature trend similar to that of the ignition delays, although characterized by a slight but continuous decline between 50-75% loading, further supporting that 62.5% TiB_2 loading accounts for the optimized condition in terms of thermite ignitability.

3.2 Thermal analysis

In order to better understand the observed trends for ignition, we investigated the low temperature condensed-phase reactions by DSC. DSC traces of various CuO/Al-TiB_2 systems are displayed in **Figure 3**. Dotted lines correspond to the DSC scans of the reference systems, CuO/Al (bottom curve) and CuO/TiB_2 (top curve). Each configuration is characterized by similar exothermic occurrences leading up to the oxidation of TiB_2 at temperatures below 500 °C and that of Al at temperatures > 500 °C as detailed in our previous work [31]. **Supporting Information, Figure S4** features a simple schematic that illustrates the progress of the reaction.

The first exotherm (onset ~ 230 °C) centered around ~ 340 °C is attributed to TiB_2 oxidation via oxygen atoms released through CuO decomposition forming TiO_x [23,37]. One of the potential mechanistic explanation of early CuO decomposition is the several highly mobile vacancies with migration activation calculated at ~0.6 eV in a previously reported study [38], created as a result of Al migration in direct contact with CuO [31]. Boron is shown to oxidize next, giving the second peak (onset ~400 °C). The endotherm at ~480 °C within the second exotherm corresponds to B_2O_3 melting. The third and the final heat release at temperatures > 500 °C is the result of Al oxidation via remaining CuO and liquid B_2O_3. CuO/Al-TiB_2 systems do not exhibit exothermic events after ~650 °C, unlike CuO/Al meaning, that the reaction occurs over a shorter extent of time. It is noteworthy that the final Al oxidation exotherm, as seen in the CuO/Al reference sample, is drastically diminished upon TiB_2 loading because Al is mostly consumed at low temperatures.

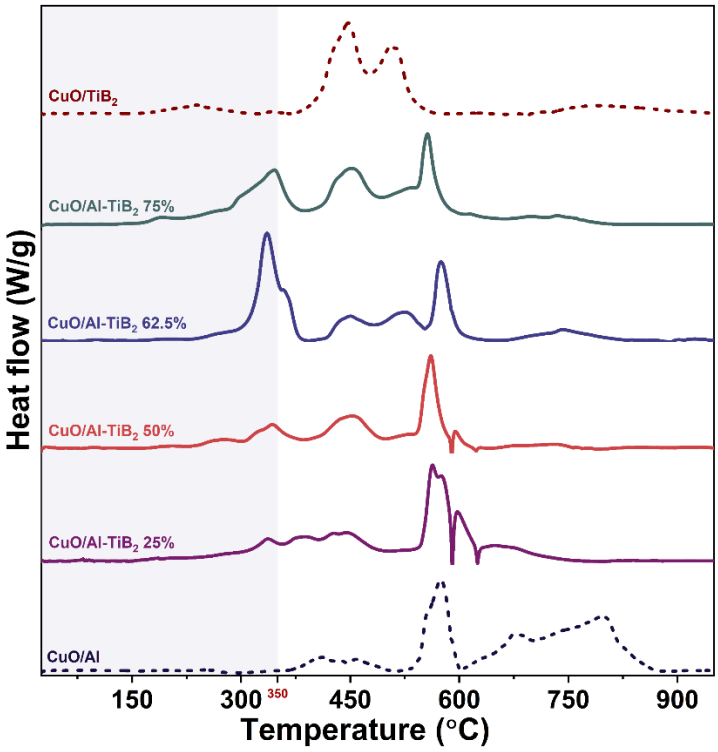

Figure 3. DSC traces recorded from each CuO/Al-TiB_2 thermite as a function of TiB_2 loading varying from 0% (CuO/Al) to 100% (CuO/TiB_2)

Table 2 summarizes the total heats of reaction of each thermite system. The theoretical heat of reaction of CuO/Al is ~3.3 kJ/g [39]. However, the literature does not contain such data on CuO/TiB_2. The theoretical heats of reaction of CuO/Al-TiB_2 are estimated using the heat release from CuO/Al and CuO/TiB_2 that has been obtained experimentally. The total heat released exhibits a considerable decrease as the TiB_2 loading varies, dropping from 1.4 kJ/g at 25% to 0.8 kJ/g at 50%, after which it shows minor variations. This phenomenon could arise due to the increasing presence of B_2O_3, leading to the formation of a surface melt composed of B_2O_3-TiO_x, which in turn hinders oxygen diffusion. The ratio of total heat released to the estimated theoretical heat (Table 2) suggest similar degree of reaction completion in different CuO/Al-TiB_2 systems. In addition, whereas each undergoes a similar sequence of reaction, it is the amount of heat released during the low

temperature exothermic events (< 350 °C, *i.e.*, onset temperature of CuO decomposition [40]) that sets them apart. The heat released increases significantly by 33% (of total expected heat ΔH_{th}) with the rise in TiB_2 content from 0% to 62.5%. 25% TiB_2 loading records a 7% low temperature heat release, while the samples with 50% TiB_2 loading released 17% of the total expected heat. This observation suggests an apparent enhancement in the superior thermal reactivity of the successive thermite configurations. Continuing to increase TiB_2 content demonstrated a slight reduction in the amount of heat released (24% for 75% TiB_2 loading) during the low temperature regime. This may either be attributed to the secondary higher order reactions or excess B_2O_3 melting. Interestingly, this distinctive behavior is clearly observed throughout the tunability of ignition delay; the more pronounced the heat released in the low temperature exotherms, the shorter the recorded ignition delay. Nevertheless, it does not imply that the heat release directly governs the ignition times. One possible explanation of such a trend could be the change in the thermal conductivity of the thermite, however the estimated thermal conductivities feature a slight decline as a function of TiB_2 loading (**Supporting Information, Table S2**). This retreats us to the conclusion that the low temperature exothermic events, indicative of the degree of heterogeneous reaction through fuel-oxidizer mixing, cannot be completely overlooked.

Table 2. Summary of the heat of reaction as a result of TiB_2 loading in CuO/Al-TiB_2

Sample name	TiB_2 loading (%)	Total heat release ΔH (kJ/g)	Theoretical heat of reaction ΔH_{th} (kJ/g)	$\Delta H/\Delta H_{th}$	Heat released below 350 °C (%)
CuO/Al	0	1.8	-	-	0.1
CuO/Al-TiB_2 25%	25	1.4	1.4	1.0	7
CuO/Al-TiB_2 50%	50	0.8	1.0	0.8	17
CuO/Al-TiB_2 62.5%	62.5	1.0	1.2	0.9	33
CuO/Al-TiB_2 75%	75	0.9	1.2	0.8	24
CuO/TiB_2	100	1.3	-	-	6

3.3 Macroscopic and microscopic combustion behavior

Macroscopic imaging: Each CuO/Al-TiB_2 system sustains continuous propagation under ambient conditions, the propagation rates plotted in **Figure 4a**. As an illustration, for each TiB_2 loading condition, one snapshot of the flame propagation is shown in **Figure 4b**. The snapshots of the flame propagation in CuO/Al and CuO/TiB_2 are shown in **Supporting Information, Figure S5**. 25% TiB_2 loading burns at 10.8 ± 0.42 $m.s^{-1}$, nearly twice as fast as CuO/Al (4.2 ± 0.1 $m.s^{-1}$), and 50%, 62.5% and 75% TiB_2 loadings propagate at 9.1 ± 0.54 $m.s^{-1}$, 10.8 ± 0.85 $m.s^{-1}$ and 8.7 ± 0.61 $m.s^{-1}$ respectively, all of which are nearly four times that of TiB_2-only sample (2.2 ± 0.04 $m.s^{-1}$).

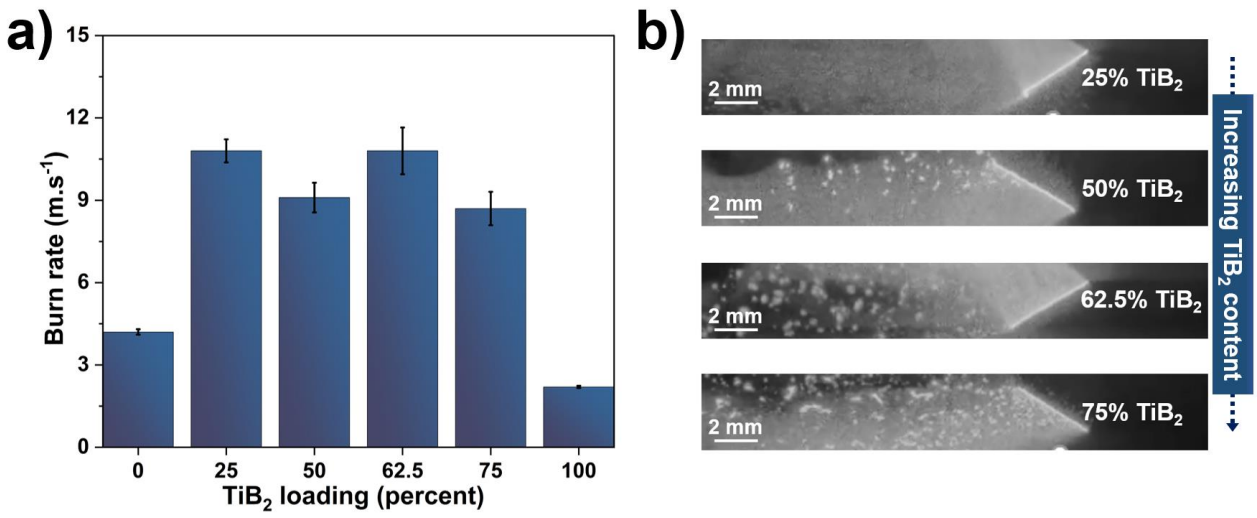

Figure 4. (a) Macroscopic burn rate of CuO/Al-TiB_2 thermites as a function of TiB_2 loading varying from 0% (CuO/Al) to 100% (CuO/TiB_2) as well as (b) macroscopic snapshots from each of the four CuO/Al-TiB_2 samples. The burning surface ejects larger and a greater number of particles as the TiB_2 concentration in CuO/Al increases. They appear to be still burning (higher brightness) even though the front has moved away along the propagation axis.

CuO/Al-TiB_2 thermites burn much faster than CuO/Al despite the low thermal diffusivity and low combustion temperature of CuO/TiB_2 (1.6×10^{-5} $m^2.s^{-1}$ and 1800 °C, respectively) in comparison to CuO/Al (2.1×10^{-5} $m^2.s^{-1}$ and 3500 °C, respectively). This brings the mechanisms controlling

the combustion dynamics in such new Al-TiB_2 based thermite into question. We know that the flame propagation in the thermite system is highly influenced by the modes of heat transfer (flux by conduction, convection, radiation and/or advection) and the reaction pathways (which include heterogeneous gas-condensed phase reaction; interfacial condensed-phase reactions e.g. oxygen and metal ions transport across two molten or solid materials; or even more complex mechanisms, especially for a ternary system). Thus, to better understand the combustion regime in Al-TiB_2 based thermite, the self-propagating reaction zone is microscopically imaged from the bottom (indirect imaging through the glass substrate) and from the top (direct imaging). From indirect microimaging observations, the flame front width and the corrugation of the flame surface is calculated as key indicators of the heat flux released during the propagation. Then from direct microimaging, burning particles in the air, fuel agglomerates burning on or in the vicinity of the surface, their shape and sizes are characterized to get insights into the combustion mechanisms. For the purpose of comparative analysis, the reference CuO/Al and CuO/TiB_2 samples were also characterized.

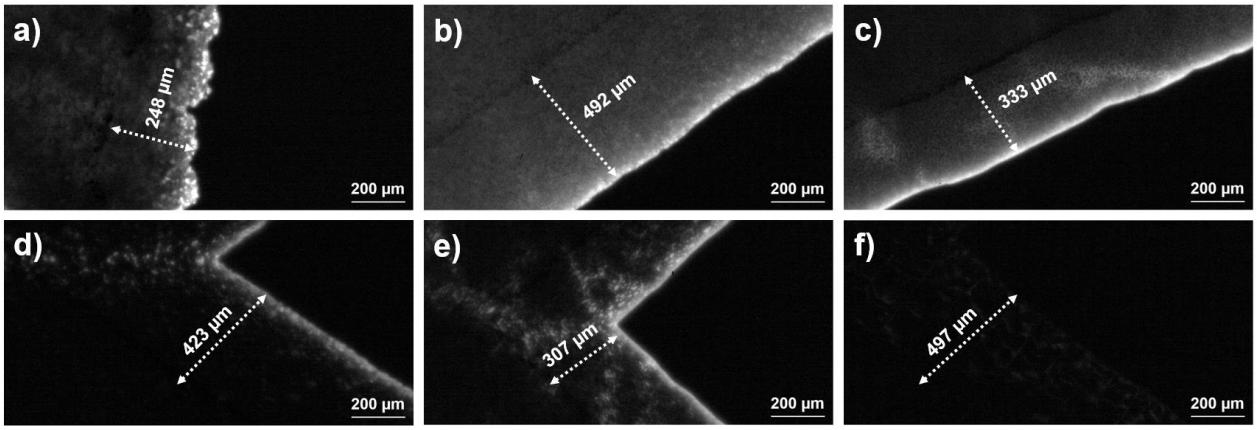

Figure 5. Microscopic snapshots (indirect imaging) of the self-propagating front in (a) CuO/Al (0 % TiB_2); CuO/Al-TiB_2 with (b) 25% TiB_2 (c) 50% TiB_2 (d) 62.5% TiB_2 (e) 75% TiB_2 and (f) CuO/TiB_2 (100% TiB_2) samples. The front width measured in each case is indicated against each micrograph

Flame front analysis from indirect microimaging: **Figure 5** shows the flame front of CuO/Al, CuO/TiB_2 and CuO/Al-TiB_2 multilayers imaged indirectly at a resolution of ~1.5 μm/px. All the optical micrographs were collected under exactly same conditions and exposure time values (1 μs). At first glance, the brightness of the self-propagating front declines as the amount of TiB_2 is increased in Al, with CuO/TiB_2 burning the dimmest. This is in direct relation with lower flame temperature for TiB_2 fuel in comparison to the Al one. The flame temperatures of CuO/Al, CuO/TiB_2 and CuO-Al-TiB_2 systems were measured at 3500 °C, 1800 °C and ~3000 °C [31].

Another striking feature is the planarity of the flame front of CuO/Al-TiB_2 samples over that of CuO/Al, which exhibits severe irregularity and corrugation. Also, CuO/Al shows a front width of ~248 μm, significantly shorter in comparison to that of CuO/Al-TiB_2 samples (492 μm for 25% TiB_2, 333 μm for 50% TiB_2, 423 μm for 62.5% TiB_2 and 307 μm for 75% TiB_2 loadings). This enlargement comes as a direct consequence of condensed-phase combustion of TiB_2 (front width of 497 μm) which extends the combustion zone upstream of the flame front. In order to characterize the burning surface area, we introduce a corrugation factor, *i.e.*, the ratio of the total geometrical length (L) of the flame to the width (W) of the sample in the direction perpendicular to the propagation. It was shown in a precedent paper [41] that the average macroscopic burn rate (BR_{macro}) can be predicted as the product of the micro-burn rate (local vector burn-rate in microscopic scale controlled by the reaction kinetics) and the corrugation (**Eq.1**). Micro-burn rates are measured from the snapshots of **Figure 5** averaging the value across multiple points on flame-front by defining a 400 × 400 squared pixel element (summarized in **Supporting Information, Figure S6**). It is assumed that each point on the front propagates to the nearest point on the next front captured through the high-speed camera. We have:

$$\boldsymbol{BR_{micro} = BR_{macro} \times \frac{W}{L}} \qquad \textbf{Eq.1}$$

where BR_{micro} and BR_{macro} represents the estimated average microscopic and measured average macroscopic burn rates respectively, L represents the measured geometrical length of the flame front and W represents the width of the sample perpendicular to the direction of the flame propagation.

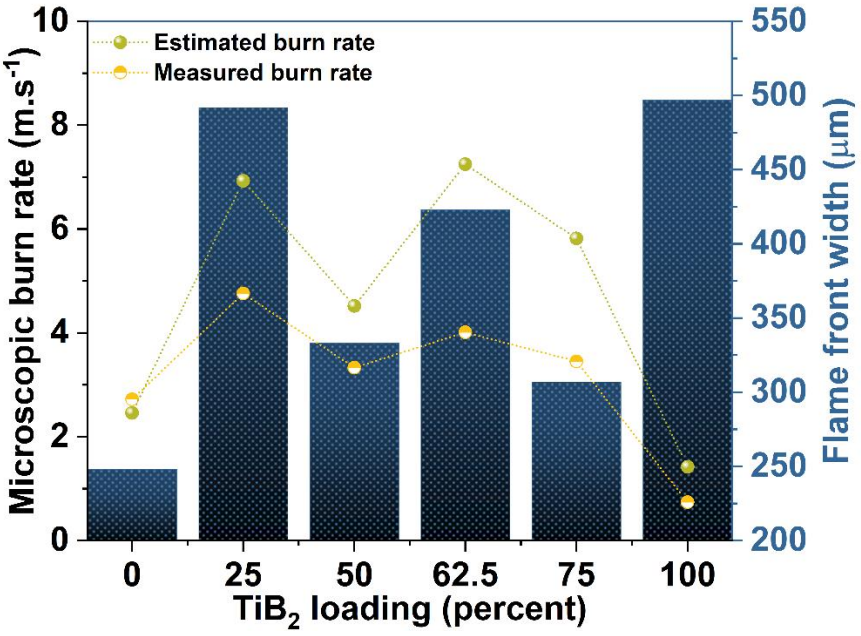

Figure 6. Microscopic burn rates (estimated and measured) as well as the respective flame front width as a function of TiB_2 loading in CuO/Al. The columns correspond to the flame front widths. 0% TiB_2 loading represents CuO/Al nanothermite and 100% TiB_2 loading represents CuO/TiB_2 ones

Figure 6 plots the variation in the measured (**Supporting Information, Figure S6**) and the estimated (from **Eq.1**) micro-burn rates as a function of TiB_2 loading. The respective values for each are summarized in **Table 3**. The corrugation increases the reaction surface area which in turn can manifest itself as an increase in the average macroscopic burn rate as observed in CuO/Al thermites [41]. In CuO/Al-TiB_2 nanothermites however, this is not found to be true. 50% TiB_2 loading sample is observed to have the maximum extent of flame corrugation, however its burn rate shows

a slight decline compared to that of 25% TiB_2 loading sample. It is worth noting that CuO/Al shows a more corrugated front compared to CuO/Al-TiB_2 samples, yet propagates much slower. Furthermore, **Eq.1** does a decent job in estimating the trend in micro-burn rates across each CuO/Al-TiB_2 configuration as well as that of the reference CuO/Al and CuO/TiB_2 samples. Nevertheless, corrugation is seemingly not the only factor, and the reasons to account for this behavior must be carefully assessed.

Table 3. Summary of flame length, sample width, observed macro and microscopic as well as calculated microscopic burn rates for CuO/Al, CuO/TiB_2 and CuO/Al-TiB_2 system

Sample name	TiB_2 loading (%)	n (molar ratio of TiB_2 and Al)	L/W Corrugation factor	Burn rate ($m.s^{-1}$)		
				Measured macroscopic	Estimated microscopic	Measured microscopic
CuO/Al	0	-	1.71	4.2	2.46	2.72
CuO/Al-TiB_2 (25%)	25	0.1	1.56	10.8	6.93	4.76
CuO/Al-TiB_2 (50%)	50	0.3	2.01	9.1	4.52	3.33
CuO/Al-TiB_2 (62.5%)	62.5	0.5	1.49	10.8	7.25	4.01
CuO/Al-TiB_2 (75%)	75	0.9	1.49	8.7	5.82	3.45
CuO/TiB_2	100	-	1.55	2.2	1.42	0.74

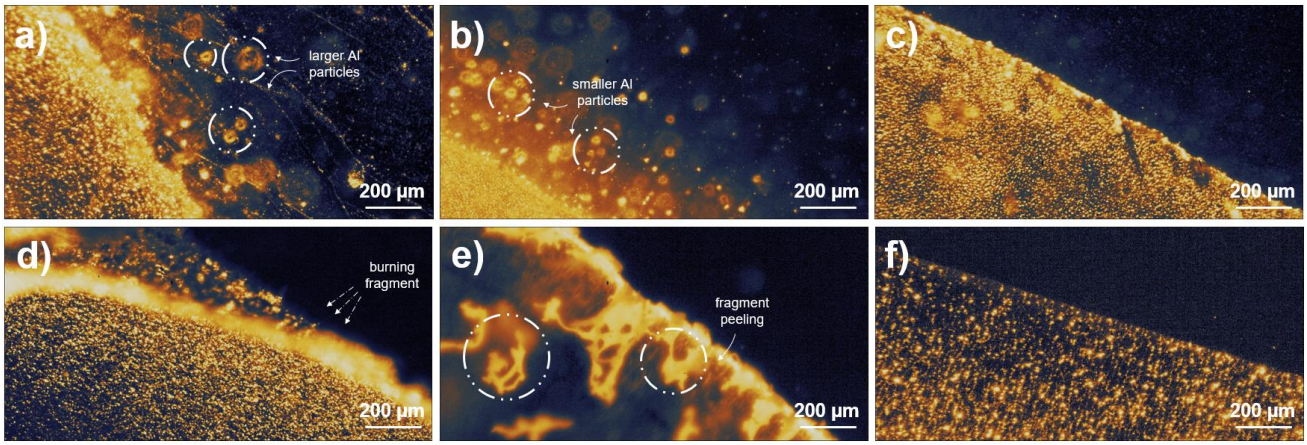

Figure 7. Microscopic snapshots (direct imaging) of the self-propagating front showing the burning surface in (a) CuO/Al (0 % TiB_2); CuO/Al-TiB_2 with (b) 25% TiB_2 (c) 50% TiB_2 (d) 62.5% TiB_2 (e) 75% TiB_2 and (f) CuO/TiB_2 (100% TiB_2) samples

Combustion regime analysis from direct microimaging: Next, we imaged the front directly from the top by placing the high-speed camera 60 mm away from the top of the sample to analyze the fuel agglomerates released from the flame. **Figure 7a-f** show the optical micrographs obtained from CuO/Al-TiB_2 samples with different TiB_2 loadings as well as the reference samples. In **Figure 7a**, corresponding to CuO/Al sample, the front is very luminous with bright spherical particles ejected from the burning surface as the front progresses. These are Al droplets which continue to burn in the atmosphere (in air) as Al melts at 660 °C and boils at 2470 °C, *i.e.*, below the estimated combustion temperature of 3300 °C. The size distribution of these agglomerates (**Figure 7a** and **Figure 8a**) is shown in **Supporting Information, Figure S7a**. The less bright region around the front is presumably alumina fumes coming from gas phase aluminum oxidation [42]. As TiB_2 loading is increased to 25%, the size of the burning Al droplets and Al/Al_2O_3 byproducts (**Figure 7b** and **Figure 8b**) decrease (particle size distribution shown in **Supporting Information, Figure S7b**) and the front becomes much evener compared to severely irregular CuO/Al front. Most notably, any further increase in TiB_2 loading no longer results in any particle ejections from the surface. Rather, the region close to the front is seen to be relatively populated with condensed matter burning on the surface which indicates solid Ti and B combustion (50 % TiB_2 loading, **Figure 7c** and **Figure 8c**). Note that B and Ti boiling points, at 3900 °C and 3260 °C respectively, are well above the flame temperature. Interestingly, 62.5% TiB_2 sample features a single and continuous burning fragment latched to the surface being dragged upstream by the propagation front (bright region marked by arrows, **Figure 7d**). Finally, 75% TiB_2 loading sample displays several porous fragments of burning material coming off of the thermite surface as the combustion progressed

(**Figure 7e**). This is an intermediate behavior between molten product ejection (Al presence, low loading) and fully condensed combustion (no Al). Indeed, CuO/TiB_2 (100% TiB_2) burns faintly without driving any residual material out (**Figure 7e**).

In summary, TiB_2 is seen to combust in condensed phase whereas Al burns in vapor phase [43] *i.e.*, molten Al droplet burns in air with the formation of a detached flame envelop producing bright spots. Vapor phase combustion is a much faster process compared to condensed phase burning limited by slow diffusion of O_2 and other species (Ti, B). Therefore, a synergistic effect between condensed phase burning of TiB_2 and vapor phase burning of Al explains the significant burn rate enhancement when TiB_2 is brought into CuO/Al: (i) Firstly, since TiB_2 does not generate any residues far away from the surface during burning, it reasonably traps Al particles to not only burn closer to the surface but also reduces agglomeration by acting as a barrier between them. This is clear from the visualization of the snapshots presented in **Figure 7a-c**. Increasing TiB_2 loading results in reducing the number of large spherical Al particles burning farther away from the front. The proximity of the flaming material close to the surface ensures higher heat feedback and less thermal losses into the environment aiding in the propagation rate. (ii) Secondly, as TiB_2 loading is increased, one can expect a higher concentration of B_2O_3. As reported before, TiB_2 tends to oxidize much before and way faster than Al in CuO/Al-TiB_2 system [31]. Under such a scenario, oxidized and condensed Cu accumulates and contributes to enhancing the front propagation due to its high thermal conductivity (348 $W.m^{-1}K^{-1}$) in comparison to that of CuO (33 $W.m^{-1}K^{-1}$). Furthermore, B_2O_3 has a melting temperature of ~450 °C while Al melts at ~600 °C. Additional heat can come from Al oxidation via B_2O_3 to release free B in the bulk. However, such a situation can only arise as a result of proper reactant mixing.

Finally, to confirm these above stated conclusions on the mechanisms that lead to an enhanced burn rate, the combustion products were collected from each sample and analyzed using SEM-EDX.

3.4 Characterization of the post-combustion product

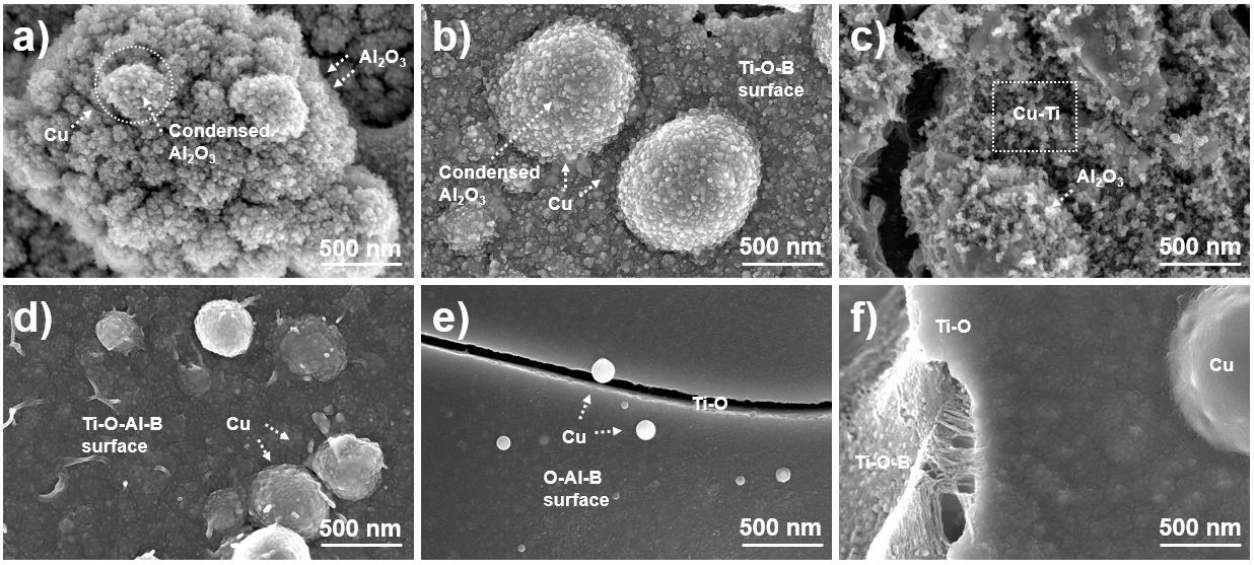

Figure 8. SEM images of post-combustion product collected from (a) CuO/Al (0% TiB_2); CuO/Al-TiB_2 with (b) 25% TiB_2 (c) 50% TiB_2 (d) 62.5% TiB_2 (e) 75% TiB_2; and (f) CuO/TiB_2 (100% TiB_2) samples

Figure 8a-f show SEM images obtained from the byproducts collected after combustion of CuO/Al, CuO/TiB_2 as well as the different CuO/Al-TiB_2 samples. The micrographs were collected from different locations across each configuration of CuO/Al-TiB_2 (and reference) samples and chemically mapped using EDX, which can be found in **Supporting Information**. As expected, the byproducts of CuO/Al display surfaces composed of large alumina agglomerates with nearly oval shaped Cu particles embedded onto it (**Figure 8a**). Some of this alumina can also be seen to condense unevenly on the surface of Cu (**Supporting Information, Figure S8**). Furthermore, the Cu surface is inhabited by several nanoparticles that show the presence of Al and O in them as

confirmed by EDX. We speculate this to be a metastable $Al_xCu_yO_z$ product in addition to Al_2O_3 owing to the rapid quenching of the products on a cold collection slide. 25% TiB_2 loading sample (**Figure 8b**) shows less alumina agglomerates with a simultaneous presence of Al-Ti on its surface (**Supporting Information, Figure S9**). Since Ti melting point (1668 °C) is much higher compared to that of Al (660 °C), it can presumably lower Al sintering by decreasing the likelihood of Al-Al coalescing, which can in turn increase contact area of Al with other species to induce faster reaction rates. Additionally, Al-Al and Al-Ti bonds carry equal probability of formation with similar bond dissociation energies (264 $kJ.mol^{-1}$ and 263 $kJ.mol^{-1}$). Notably, several small B clusters were seen on top of larger Al-Ti and Cu particles (**Supporting Information, Figure S9**). **Figure S10** (**Supporting Information**) shows the matter ejected from the burning zone, which consists of a Cu head, followed by Al-Ti-O tail decorated non-homogeneously with B. The product morphology changes considerably in 50% TiB_2 sample (**Figure 8c**) where large Cu grains are decorated with small Ti ones (**Supporting Information, Figure S11**). Within the experimental limits of EDX, B seemingly segregates to the grain boundaries of Cu, embedded into severely cracked alumina surface confirming the B clustering stage during TiB_2 oxidation [44]. As for the fragmented condensed matter (**Figure 7c**), **Supporting Information, Figure S12** shows it to be alumina tenanted by micron sized Cu particles and fewer Ti particles. B shows little clustering in the vicinity of Cu grain boundaries. Increasing TiB_2 further to 62.5% gives several perfectly spherical Cu nanoparticles (<100 nm in size) and a few Al_2O_3 embedded in Ti-Al-O-B surface (**Supporting Information, Figure S13**). The surface shows uneven and continuous thin-film peeling (**Supporting Information, Figure S14a**), as seen in the high-speed snapshot from this sample (**Figure 7d**). The solid fragment collected (**Supporting Information, Figure S14b-c**) contains mostly metallic Cu and alumina. As for 75% TiB_2 loading, there is a distribution of widely cracked planar surfaces (**Figure 8e**) and quenched molten product. The EDX analysis reveals a surface

covered in oxides of B with nano size Cu particles engrained into it. A simultaneous and uneven occurrence of Al-Ti-O is also recorded (**Supporting Information, Figure S15a-b**). Finally, CuO/TiB_2 displays some interesting sintering among Ti-B-O containing grains **(Supporting Information, Figure S16)**. The multilayer also shows excessive crack development post combustion with few hundreds of nm scale Cu particles seated in a pool of Ti-O-B with B segregation towards the boundaries of the cracks (**Supporting Information, Figure S17**). Due to the presence in the quenched product we conjecture that B_2O_3 never reached its boiling temperature in this regime. Additionally, given the low flame temperature and unduly non-luminosity, we hypothesize incomplete combustion in this sample. Overall, these observations confirm the scenario presented in Section 3.3. TiB_2 combustion forms B_2O_3 (and TiO_x) which, until its boiling point (1860 °C) acts as a trap for Al droplets impeding the latter's escape from the surface. It raises the local temperature and enhances the flame propagation rate by facilitating the heat feedback to the unburnt material. Furthermore, Al burning in the gas phase assists in increasing the burning surface as well as raising the combustion temperature (~3000 °C for Al-TiB_2 samples against 1800 °C for TiB_2-only samples) leading to the formation of several Cu nanoparticles, which in turn due to their higher thermal conductivity, help achieve faster flame propagation rates. B_2O_3 melt can either segregate to the grain boundaries, or remain in bulk and cause hinderance to atomic diffusion, as seen in CuO/TiB_2 samples. With Al present in the system, the former phenomenon occurs and thus CuO/Al-TiB_2 samples exhibit higher propagation rates compared to TiB_2-only thermites.

4. Conclusion

By systematically incorporating nano-TiB_2 into CuO/Al and adjusting the bi-fuel distribution between Al-TiB_2 through TiB_2 loading (25%, 50%, 62.5% and 75%), CuO/Al-TiB_2 multilayers were fabricated using magnetron sputtering. The study of their ignition points revealed that loading

TiB_2 into CuO/Al thermite decreases the ignition delay, with a minimum at 62.5% (0.08 ms): a notable ~3-orders of improvement from the reference CuO/Al sample. Examining the low temperature redox reactions using DSC, TiB_2 showed superior oxygen affinity compared to Al. Despite each CuO/Al-TiB_2 multilayer being characterized by a similar degree of reaction completeness and the same order of thermal conductivities, the samples with 62.5% loading exhibited superior reactivity. It released 33% of the expected heat of reaction below 350 °C, highest among all. Then a combination of high-speed videography and SEM-EDX permitted to investigate the combustion regime of ternary CuO/Al-TiB_2 nano-thermites. Two main observations can be highlighted as the factors contributing to the positive synergistic effect between TiB_2-condensed phase burning and Al-vapor phase combustion, resulting in a twofold enhancement in the burn rate when TiB_2 is introduced into CuO/Al. In CuO/Al-TiB_2, the Al droplets burn closer to the surface ensuring an effective heat feedback to the unburnt material to sustain propagation, compared to CuO/Al wherein the particles burn away from the surface causing heat losses. This is primarily due to the B_2O_3 surface melt created as a result of TiB_2 oxidation. Furthermore, TiB_2-rich samples (loading > 62.5%) showed a higher presence of small sized Cu nanoparticles (<100 nm), owing to a relatively faster TiB_2 oxidation, that then facilitates propagation due to its high thermal conductivity. This work introduced an accessible method for preparing Al-based nano-laminates with tunable reactivity and additionally, elucidates the factors contributing to the improved ignition and combustion behavior resulting from nano-TiB_2 addition.

Supporting Information

Sputtering process conditions; Details on the device and experimental setup; Pictures of combustion product residues collected on glass slides after propagation; Schematic of the reaction steps in Al-TiB_2/CuO laminates; Imaging snapshots of propagating combustion in Al/CuO and

TiB_2/CuO; Detail of micro-burn rate calculation; Distribution of particles size of combustion residues collected on glass slide; Physical and thermal properties of Al-TiB_2/CuO nanolaminates with different Al:TiB_2 ratios; SEM images and EDX maps of quenched Al-TiB_2/CuO nanolaminates surface with different Al:TiB_2 ratios; The Supporting Information is available free of charge on the ACS Publications website at DOI:

Funding Sources

C.R. received funding from the European Research Council (ERC) under the European Union's Horizon 2020 research and innovation program (grand agreement No. 832889 - PyroSafe).

Notes

The authors declare that they have no known competing financial interests or personal relationships that could have appeared to influence the work reported in this paper.

Acknowledgements

The authors gratefully acknowledge the support from the European Research Council (H2020 Excellent Science) Researcher Award (grant 832889 – PyroSafe). This work was also supported by LAAS-CNRS technology platform, a member of Renatech network. The authors acknowledge the help from Claudie Josse for SEM sample preparations and observations as well as from Wilfried Quelin of Photonlines Solution Optiques for loan and assistance on Cavilux HF systems.

References:

(1) Valdes, J. J.; Potember, R. S.; Kotras, D. M. Nanoenergetic Materials for Microscale Tactical Applications. Army University Press. https://www.armyupress.army.mil/Journals/Military-Review/Online-Exclusive/2023-OLE/nanoenergetic/

(2) Rossi, C. Metallized reactive materials – a road to clean and sustainable pyrotechnics. *Propellants Explos. Pyrotech.* **2023**, *48.*

(3) Weihs, T. P. Applications of Reactive Multilayer Foils. In *Concise Encyclopedia of Self-Propagating High-Temperature Synthesis*; *Elsevier* **2017**; 19–21.

(4) Glavier, L.; Nicollet, A.; Jouot, F.; Martin, B.; Barberon, J.; Renaud, L.; Rossi, C. Nanothermite/RDX-Based Miniature Device for Impact Ignition of High Explosives. *Propellants Explos. Pyrotech.* **2017**, *42*, 308–317.

(5) Xu, J.; Tai, Y.; Shen, Y.; Dai, J.; Xu, W.; Ye, Y.; Shen, R.; Hu, Y. Characteristics of Energetic Semiconductor Bridge Initiator Based on Different Stoichiometric Ratios of Al/MoO3 Reactive Multilayer Films under Capacitor Discharge Conditions. *Sens. Actuators, A Phys*. **2019**, *296*, 241–248.

(6) Nellums, R. R.; Son, S. F.; Groven, L. J. Preparation and Characterization of Aqueous Nanothermite Inks for Direct Deposition on SCB Initiators. *Propellants Explos. Pyrotech.* **2014**, *39*, 463–470.

(7) Nicollet, A.; Salvagnac, L.; Baijot, V.; Estève, A.; Rossi, C. Fast Circuit Breaker Based on Integration of Al/CuO Nanothermites. *Sens. Actuators, A Phys*. **2018**, *273*, 249–255.

(8) Wu, T.; Sevely, F.; Julien, B; Sodre, F.; Cure, J.; Tenailleau, C.; Esteve,C.; Rossi, C. New coordination complexes-based gas-generating energetic composites. *Combust. Flame.* **2020**, *219*, 478-487.

(9) Ervin, M. H.; Bedair, S. S.; Knick, C. R.; Tsang, H.; Isaacson, B.; Piekiel, N. W. Evaporation Driven Assembly of On-Chip Thermite Devices. *J Microelectromech Syst* **2017**, *26*, 1408–1416.

(10) Pandey, S. S.; Banerjee, N.; Xie, Y.; Mastrangelo, C. H. Self-Destructing Secured Microchips by On-Chip Triggered Energetic and Corrosive Attacks for Transient Electronics. *Adv. Mater. Technol.* **2018**, *3*, 1800044.

(11) Salvagnac, L.; Assie-Souleille, S.; Rossi, C. Layered Al/CuO Thin Films for Tunable Ignition and Actuations. *Nanomaterials* **2020**, *10*, 2009.

(12) Ru, C.; Wang, F.; Xu, J.; Dai, J.; Shen, Y.; Ye, Y.; Zhu, P.; Shen, R. Superior Performance of a MEMS-Based Solid Propellant Microthruster (SPM) Array with Nanothermites. *Microsyst Technol* **2017**, *23*, 3161–3174.

(13) Apperson, S. J.; Bezmelnitsyn, A. V.; Thiruvengadathan, R.; Gangopadhyay, K.; Gangopadhyay, S.; Balas, W. A.; Anderson, P. E.; Nicolich, S. M. Characterization of Nanothermite Material for Solid-Fuel Microthruster Applications. *J. Propuls. Power* **2009**, *25*, 1086–1091.

(14) Chaalane, A.; Rossi, C.; Estève, D. The Formulation and Testing of New Solid Propellant Mixture (DB+x%BP) for a New MEMS-Based Microthruster. *Sens. Actuators, A Phys*. **2007**, *138*, 161–166.

(15) Williams, A.; Shancita, I.; Altman, I.; Tamura, N.; Pantoya, M. L. On the Pressure Generated by Thermite Reactions Using Stress-Altered Aluminum Particles. *Propellants Explos. Pyrotech.* **2021**, *46*, 99–106.

(16) Miller, K. K.; Gottfried, J. L.; Walck, S. D.; Pantoya, M. L.; Wu, C.C. Plasma Surface Treatment of Aluminum Nanoparticles for Energetic Material Applications. *Combust. Flame.* **2019**, *206*, 211–213.
(17) Julien, B.; Cure, J.; Salvagnac, L.; Josse, C.; Esteve, A.; Rossi, C. Integration of Gold Nanoparticles to Modulate the Ignitability of Nanothermite Films. *ACS Appl. Nano Mater.* **2020**, *3*, 2562–2572.
(18) He, W.; Li, Z.-H.; Chen, S.; Yang, G.; Yang, Z.; Liu, P.-J.; Yan, Q.L. Energetic Metastable N-Al@PVDF/EMOF Composite Nanofibers with Improved Combustion Performances. *Chem. Eng. J.* **2020**, *383*, 123146.
(19) DeLisio, J. B.; Hu, X.; Wu, T.; Egan, G. C.; Young, G.; Zachariah, M. R. Probing the Reaction Mechanism of Aluminum/Poly(Vinylidene Fluoride) Composites. *J. Phys. Chem. B* **2016**, *120*, 5534–5542.
(20) Wu, T.; Wang, X.; DeLisio, J. B.; Holdren, S.; Zachariah, M. R. Carbon Addition Lowers Initiation and Iodine Release Temperatures from Iodine Oxide-Based Biocidal Energetic Materials. *Carbon* **2018**, *130*, 410–415.
(21) Marín, L.; Gao, Y.; Vallet, M.; Abdallah, I.; Warot-Fonrose, B.; Tenailleau, C.; Lucero, A. T.; Kim, J.; Esteve, A.; Chabal, Y. J.; Rossi, C. Performance Enhancement via Incorporation of ZnO Nanolayers in Energetic Al/CuO Multilayers. *Langmuir* **2017**, *33*, 11086–11093.
(22) Zhao, W.; Wang, X.; Wang, H.; Wu, T.; Kline, D. J.; Rehwoldt, M.; Ren, H.; Zachariah, M. R. Titanium Enhanced Ignition and Combustion of Al/I2O5 Mesoparticle Composites. *Combust. Flame.* **2020**, *212*, 245–251.
(23) Wu, T.; Singh, V.; Julien, B.; Tenailleau, C.; Estève, A.; Rossi, C. Pioneering Insights into the Superior Performance of Titanium as a Fuel in Energetic Materials. *Chem. Eng. J.* **2023**, *453*, 139922.
(24) Liu, X.; Chintersingh, K.-L.; Schoenitz, M.; Dreizin, E. L. Reactive Composite Boron–Magnesium Powders Prepared by Mechanical Milling. *J. Propuls. Power* **2018**, *34*, 787–794.
(25) Zhao, W.; Wang, H.; Kline, D. J.; Wang, X.; Wu, T.; Xu, J.; Ren, H.; Zachariah, M. R. Influence of Titanium Addition on Performance of Boron-Based Thermites. *Chem. Eng. J.* **2022**, 134837.
(26) Wang, X.; Wu, T.; Wang, H.; DeLisio, J. B.; Yang, Y.; Zachariah, M. R. Boron Ignition and Combustion with Doped δ-Bi2O3: Bond Energy/Oxygen Vacancy Relationships. *Combust. Flame.* **2018**, *197*, 127–133.
(27) Dreizin, E. L. Metal-Based Reactive Nanomaterials. *Prog. Energy Combust.* **2009**, *35*, 141–167.
(28) Jain, A.; Joseph, K.; Anthonysamy, S.; Gupta, G. S. Kinetics of Oxidation of Boron Powder. *Thermochim. Acta* **2011**, *514*, 67–73.
(29) Devener, B. V.; Perez, J. P. L.; Jankovich, J.; Anderson, S. L. Oxide-Free, Catalyst-Coated, Fuel-Soluble, Air-Stable Boron Nanopowder as Combined Combustion Catalyst and High Energy Density Fuel. *Energy Fuels* **2009**, 23, 6111-6120.
(30) Sullivan, K.; Young, G.; Zachariah, M. R. Enhanced Reactivity of Nano-B/Al/CuO MICs. *Combust. Flame.* **2009**, *156*, 302–309.
(31) Singh, V.; Wu, T.; Hagen, E.; Salvagnac, L.; Tenailleau, C.; Estéve, A.; Zachariah, M. R.; Rossi, C. How Positioning of a Hard Ceramic TiB2 Layer in Al/CuO Multilayers Can Regulate the Overall Energy Release Behavior. *Fuel* **2023**, *349*, 128599.
(32) Pivkina, A. N.; Meerov, D. B.; Monogarov, K. A.; Frolov, Yu. V.; Muravyev, N. V. Prospects of Using Boron Powders As Fuel. II. Influence of Aluminum and Magnesium

Additives and Their Compounds on the Thermal Behavior of Boron Oxide. *Combust Explos Shock Waves* **2020**, *56*, 148–155.
(33) Mursalat, M.; Huang, C.; Julien, B.; Schoenitz, M.; Esteve, A.; Rossi, C.; Dreizin, E. L. Low-Temperature Exothermic Reactions in Al/CuO Nanothermites Producing Copper Nanodots and Accelerating Combustion. *ACS Appl. Nano Mater.* **2021**, 4, 3811-3820.
(34) Jabraoui, H.; Djafari Rouhani, M.; Rossi, C.; Esteve, A. First-Principles Investigation of CuO Decomposition and Its Transformation into Cu2O. *Phys. Rev. Mater.* **2022**, *6*, 096001.
(35) Jian, G.; Zhou, L.; Piekel, N.W.; Zachariah, M. R. Low Effective Activation Energies for Oxygen Release from Metal Oxides: Evidence for Mass-Transfer Limits at High Heating Rates. *ChemPhysChem **2014**, 15, 1666-1672.*
(36) Singh, V.; Julien, B.; Salvagnac, L,; Pelloquin, S.; Hungria, T.; Josse, C.; Belhaj, M.; Rossi, C. Influence of Process Parameters on Energetic Properties of Sputter-Deposited Al/CuO Reactive Multilayers. *Nanotechnology* **2022**, 33, 465704.
(37) Jabraoui, H.; Estève, A.; Hong, S.; Rossi, C. Initial Stage of Titanium Oxidation in Ti/CuO Thermites: A Molecular Dynamics Study Using ReaxFF Forcefields. *Phys. Chem. Chem. Phys.* **2023**, *25*, 11268–11277.
(38) Ono, K.; Kino, T. Migration Energy of Mono-Vacancy in Aluminum at High Temperature. *J. Phys. Soc. Jpn.* **1978**, *44*, 875–881.
(39) Petrantoni, M.; Rossi, C.; Salvagnac, L.; Conédéra, V.; Estève, A.; Tenailleau, C.; Alphonse, P.; Chabal, Y. J. Multilayered Al/CuO Thermite Formation by Reactive Magnetron Sputtering: Nano versus Micro. *J. Appl. Phys.* **2010**, *108*, 084323.
(40) Abdallah, I.; Zapata, J.; Lahiner, G.; Warot-Fonrose, B.; Cure, J.; Chabal, Y.; Esteve, A.; Rossi, C. Structure and Chemical Characterization at the Atomic Level of Reactions in Al/CuO Multilayers. *ACS Appl. Energy Mater.* **2018**, *1*, 1762–1770.
(41) Wang, H.; Julien, B.; Kline, D. J.; Alibay, Z.; Rehwoldt, M. C.; Rossi, C.; Zachariah, M. R. Probing the Reaction Zone of Nanolaminates at ∼μs Time and ∼μm Spatial Resolution. *J. Phys. Chem. C* **2020**, *124*, 13679–13687.
(42) Dreizin, E. L. Experimental study of stages in aluminum particle combustion in air. *Combust. Flame.* **1996**, *105*, 541–556.
(43) Emelyanov, V. N.; Teterina, I. V.; Volkov, K. N. Dynamics and Combustion of Single Aluminium Agglomerate in Solid Propellant Environment. *Acta Astronaut.* **2020**, *176*, 682–694.
(44) Jabraoui, H.; Alpuche, A.; Rossi, C.; Esteve, A. New Insights into the Mechanisms of TiB2(001) Thermal Oxidation Combining Molecular Dynamics and Density Functional Theory Calculations. *Acta Mater.* **2024**, *262*, 119463.

For Table of Contents Only